Discovery of two neighbouring satellites in the Carina constellation with MagLiteS

G. Torrealba,[1,2]★ V. Belokurov,[1,3] S. E. Koposov,[1,4] K. Bechtol,[5] A. Drlica-Wagner,[6] K. A. G. Olsen,[7] A. K. Vivas,[8] B. Yanny,[9] P. Jethwa,[1] A. R. Walker,[8] T. S. Li,[9] S. Allam,[6] B. C. Conn,[10] C. Gallart,[11,12] R. A. Gruendl,[13,14] D. J. James,[15] M. D. Johnson,[14] K. Kuehn,[16] N. Kuropatkin,[9] N. F. Martin,[17,18] D. Martinez-Delgado,[19] D. L. Nidever,[7] N. E. D. Noël,[20] J. D. Simon,[21] G. S. Stringfellow[22] and D. L. Tucker[6]

Affiliations are listed at the end of the paper

ABSTRACT

We report the discovery of two ultra-faint satellites in the vicinity of the Large Magellanic Cloud (LMC) in data from the Magellanic Satellites Survey (MagLiteS). Situated 18 deg (∼20 kpc) from the LMC and separated from each other by only 18 arcmin, Carina II and III form an intriguing pair. By simultaneously modelling the spatial and the colour–magnitude stellar distributions, we find that both Carina II and Carina III are likely dwarf galaxies, although this is less clear for Carina III. There are in fact several obvious differences between the two satellites. While both are well described by an old and metal poor population, Carina II is located at ∼36 kpc from the Sun, with $M_V \sim -4.5$ and $r_h \sim 90$ pc, and it is further confirmed by the discovery of 3 RR Lyrae at the right distance. In contrast, Carina III is much more elongated, measured to be fainter ($M_V \sim -2.4$), significantly more compact ($r_h \sim 30$ pc), and closer to the Sun, at ∼28 kpc, placing it only 8 kpc away from Car II. Together with several other systems detected by the Dark Energy Camera, Carina II and III form a strongly anisotropic cloud of satellites in the vicinity of the Magellanic Clouds.

Key words: Galaxy: halo – galaxies: dwarf – Magellanic Clouds.

1 INTRODUCTION

Over the past several decades, the quest for ultra-faint Milky Way satellite galaxies has been driven by large, multipurpose digital sky surveys. The Sloan Digital Sky Survey (SDSS; York et al. 2000) and the Dark Energy Survey (DES; DES Collaboration 2005) have greatly advanced our understandin g of the ultra-faint galaxy population; however, neither survey was targeted with this science goal in mind. Thus, one of the most promising regions for finding ultra-faint galaxies has remained largely unexplored. The region around the Magellanic Clouds is expected to be littered with small satellites as a byproduct of hierarchical galaxy formation (e.g. D'Onghia & Lake 2008; Springel et al. 2008; Nichols et al. 2011; Sales et al. 2011; Wetzel, Deason & Garrison-Kimmel 2015). Indeed, the recent discovery of a large number of ultra-faint galaxies in DES data near the Clouds has provided strong support for this hypothe-

sis (Bechtol et al. 2015; Drlica-Wagner et al. 2015; Kim & Jerjen 2015b; Koposov et al. 2015).

The peculiar alignment of (some of) the DES satellites with the Large and Small Magellanic Clouds (LMC and SMC) has been scrutinized in several studies. As first pointed out by Koposov et al. (2015), under the assumption of isotropy, an overdensity of nine objects around the LMC – as revealed in the DES Year 1 imaging – is unlikely to occur by chance. This conclusion is echoed by Drlica-Wagner et al. (2015), who support their conclusion with the discovery of eight additional satellites in an adjacent part of the sky. Deason et al. (2015) study the accretion of LMC analogues in a suite of cosmological zoom-in simulations of a Milky Way-mass halo and point out that an excess of satellites around the Clouds would imply recent accretion of the Magellanic system on to the Galaxy. A different approach is taken by Jethwa, Erkal & Belokurov (2016, hereafter J16), who model the distribution of objects within the DES footprint as a mixture of the virialized Milky Way population and the accreted satellites of Magellanic origin. Instead of relying on a small number of cosmological simulations with

satellites broadly resembling the LMC (e.g. Sales et al. 2011; Deason et al. 2015; Sales et al. 2017), they follow Nichols et al. (2011) to create a framework within which the observed properties of the Clouds are reproduced. The model includes the response of the Galaxy to the in-fall of its most massive satellites (e.g. Gómez et al. 2015), as well as the dynamical friction experienced by the LMC and SMC (e.g. Kallivayalil et al. 2013). By accounting for selection biases, marginalizing over the observational errors and, most importantly, by using a fully probabilistic approach, J16 demonstrate that between one-third and one-half of the dwarfs discovered in the DES could have been delivered by the LMC.

According to the model of J16, before accretion on to the Galaxy, the LMC could have harbored as many as ∼70 faint dwarf satellites. Because the Clouds have only recently been accreted on to the Milky Way, many of their stripped sub-systems have not had much time to scatter across the sky. As J16 show, even if they have already been tidally stripped from the LMC, many of the satellites with Magellanic origins are still to be found in its vicinity. Given that a difference in energy and angular momentum exists between the LMC and its satellites, some time after gravitational release the latter will have moved along the progenitor's orbit, thus populating leading and trailing arms of tidal debris. The extent and the overall density of the clouds of stripped satellites around the LMC and the SMC can be used to place stringent constraints on the masses of the Magellanic Clouds as well as their orbital history in the Milky Way potential. Additionally, the census of the Magellanic satellites would enable a unique approach to deciphering low-mass structure emergence, perhaps shedding unexpected new light on the nature of the so-called ultra-faint dwarfs (see e.g. D'Onghia & Lake 2008; Belokurov 2013).

It is with these ideas in mind that the Magellanic SatelLites Survey (MagLiteS) was conceived. MagLiteS covers a previously unexplored region of the Magellanic neighbourhood outside of the DES footprint. The survey uses the Dark Energy Camera (DECam; Flaugher et al. 2015) on the Blanco 4 m telescope at Cerro Tololo Inter-American Observatory in Chile to map ∼1200 deg^2 near the south celestial pole. In this context, Drlica-Wagner et al. (2016a) announced the discovery of the Pictor II satellite in Run 1 of MagLiteS, comprising roughly one-quarter of the expected MagLiteS data set. Note that according to the best-fitting model reported by J16, once the survey is completed, a total of ∼5 satellites are expected, of which ∼4 should be from the Magellanic Clouds.

In this paper, we present the discovery of two additional satellites in the imaging procured by MagLiteS: Carina II and III. Curiously, these two new ultra-faint objects form a tight pair on the sky, sitting within 18 arcmin of each other. The pair also appears relatively close along the line of sight: their 3D separation is ∼8 kpc, while the two are ∼30 kpc from the Milky Way and ∼18 kpc from the LMC. Thus, it is reasonable to ask whether there is or was any physical association between them, and/or with the LMC. Naturally, before any link between the galaxies is claimed, spectroscopic follow-up is required. Additionally, we can use the J16 predictions for the satellite's line-of-sight velocity to address their association with the Magellanic Clouds.

Note, however, that despite the rigour and the complexity of the analysis presented in J16, they fail to reproduce the details of the DES satellite distribution. Broadly speaking, the spatial density model does not describe the data well on angular scales of ∼10 deg. The mismatch between the data and the model is largest at lower Magellanic latitudes, or B_{MS}, as defined in the coordinate system linked to the gaseous Magellanic Stream (see Nidever, Majewski & Burton 2008). On closer inspection, it appears that a substantial

number of DES satellites are arranged in what resembles a planar configuration. This structure contains seven DES satellites as well as the LMC and the SMC. The thickness of this slab-like distribution is <3 kpc, but the extent is 90 kpc. J16 estimate that there is a 5 per cent probability for this arrangement to happen by chance. Remarkably, all three recent discoveries by MagLiteS, i.e. Pic II (Drlica-Wagner et al. 2016a) and Carina II and III reported here, lie very close to the plane uncovered by J16.

Our findings on Carina II and III are presented in two separate papers concentrating on the photometric and spectroscopic analysis, respectively. This work (Paper I) is organized as follows: in Section 2 we describe the MagLiteS data and give the details of the discovery. Section 3 describes additional observations acquired with DECam and the time series analysis of these data. Section 4 presents the structural and stellar population modelling of the two new satellites. Finally, Section 5 discusses the possible origin of the Car II and III pair. The spectroscopic characterization of Carina II and III is presented in Li et al. (in preparation).

2 DISCOVERY

2.1 MagLites data

In this paper, we use *g*- and *r*-band data from the first MagLiteS observing run (R1) taken over six half-nights between 2016 February 10 and 2016 February 15. These data were reduced and processed by the DES Data Management system using the pipeline developed for the year-three annual reprocessing of the DES data (Sevilla et al. 2011; Mohr et al. 2012; Morganson et al., in preparation). Source detection and photometry were performed on a per exposure basis using the PSFEX and SEXTRACTOR routines (Bertin & Arnouts 1996; Bertin 2011). Astrometric calibration was performed against the UCAC-4 catalogue (Zacharias et al. 2013) using SCAMP (Bertin 2006). The SEXTRACTOR source detection threshold was set to detect sources with $S/N \gtrsim 5$. Photometric fluxes and magnitudes refer to the SEXTRACTOR PSF model fit. The median 10σ limiting depth of MagLiteS is $\gtrsim 23$ mag in both bands, which is roughly comparable to the first 2 yr of imaging by DES (Drlica-Wagner et al. 2015).

Cross-matched catalogues were assembled by performing a 1 arcsec match on objects detected in individual exposures. Stellar objects were selected based on the spread_model quantity: |wavg_spread_model_r| < 0.003 + spreaderr_model_r (see e.g. Drlica-Wagner et al. 2015; Koposov et al. 2015, for details).

Photometric calibration was performed by matching stars to the APASS catalogue on a CCD-by-CCD basis (Drlica-Wagner et al. 2015). Extinction from interstellar dust was calculated for each object from a bilinear interpolation of the extinction maps of Schlegel, Finkbeiner & Davis (1998). We followed the procedure of Schlafly & Finkbeiner (2011) to calculate reddening, assuming $R_V = 3.1$; however, in contrast to Schlafly & Finkbeiner (2011), we used a set of $A_b/E(B-V)$ coefficients derived by DES for the *g* and *r* bands: $A_g/E(B-V) = 3.683$ and $A_r/E(B-V) = 2.605$.

2.2 Discovery

Carina II and III were discovered by applying a version of the satellite search algorithm described in Torrealba et al. (2016b) to the MagLiteS data. In short, the algorithm computes the local stellar density and an estimate of the local background by convolving the star count map with two two-dimensional Gaussian kernels. A large

kernel with $\sigma_o = 60$ arcmin is used for the background estimation, which is then subtracted from a suite of 5 different small kernels with $\sigma_i = 1, 2, 5, 8'$, or 10 arcmin used for the local density estimation. Different σ_i are used to detect satellites of different apparent sizes, since the search is more sensitive to overdensities with extents similar to that of the kernel (Koposov et al. 2008). Prior to spatial convolution, we select stars using an isochrone mask that picks out a specific stellar population at a particular distance. In the analysis presented here, we use a single PARSEC isochrone (Bressan et al. 2012) with [Fe/H] = −2 and an age of ∼12 Gyr. To detect stellar systems at different distances, the isochrone is shifted to 36 different distance moduli between $16 \leq m - M \leq 23$, corresponding to satellites with heliocentric distances between $\sim16 \leq D \leq 400$ kpc. The significance, S, of an overdensity is then estimated by comparing the results of the convolution with the expected variance.

In the current implementation, we also derive a local significance to calibrate candidate identification in areas where the variance is underestimated. This is particularly relevant for the MagLiteS data set, given its proximity to the LMC – a portion of the sky with a highly variable background. Rapid fluctuations in the stellar density field break the assumptions underlying the overdensity search as described above, and bias the estimates of the local background and its variance. To avoid a large number of false positives in areas close to the LMC, we introduce the local significance, S_{L}, based on the properties of S around an overdensity:

$$S_{\mathrm{L}} = \frac{S(0) - \left\langle S_{\mathrm{d} < \sigma_o} \right\rangle}{\sqrt{\mathrm{Var}\left(S_{\mathrm{d} < \sigma_o}\right)}}, \qquad (1)$$

where $S(0)$ is the significance at the centre of an overdensity, and $S_{\mathrm{d} < \sigma_o}$ are the significance for all pixels within σ_o from the centre. In areas where the variance is underestimated, S is overestimated and then $\left\langle S_{\mathrm{d} < \sigma_o} \right\rangle \gg 0$, which means $S_{\mathrm{L}} \ll S$. This allows us to cull false positives by simply selecting overdensities that have both large S and large S_{L}.

Fig. 1 displays the values of S and S_{L} for all overdensities that pass our minimum significance cut and are located sufficiently far from both the Galactic plane ($|b| > 12$ deg) and the LMC ($D_{\mathrm{LMC}} > 10°$). Previously known objects are shown in blue, while unidentified candidates are shown as black points. In grey we show a small number of overdensities associated with obvious data arte-facts that had to be removed manually[1]. The two newly discovered objects that are the focus of this paper are shown in red. These systems are both located in the constellation of Carina, which already hosts a classical dwarf spheroidal galaxy (Cannon, Hawarden & Tritton 1977), and therefore are assigned the names Carina II and Carina III. In the list from which we pick trustworthy satellite candidates with $S_{\mathrm{L}} > 6$, Car II appears as the most significant detection with $S = 9.9$, and Car III as the second most significant detection, with $S = 7.6$. On the sky, the two are very close to each other, only ∼18 arcmin apart, but are detected as two distinct overdensities by our algorithm. Other candidates above the $S_{\mathrm{L}} = 6$ line are not obviously spurious nor obviously real, so more analysis/data is needed to confirm or discard them.

The left-hand panel of Fig. 2 shows the density distribution of the main sequence turn-off (MSTO) stars in the area around Carinas. The MSTO stars are selected with an isochrone mask based on an

---

[1] These are easy to identify and removed due to their rectangular CCD chip-like shapes.
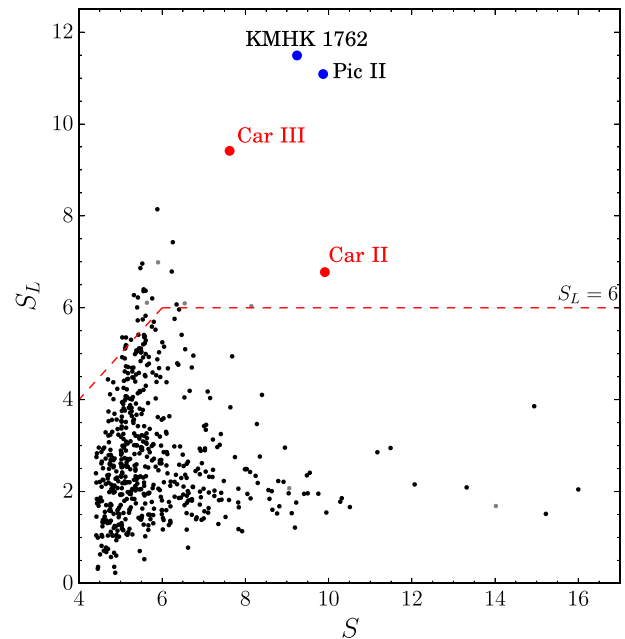
Figure 1. Stellar overdensity significance versus 'local' significance (see the main text for details) of MagLiteS candidate detections. Only stars with $|b| > 12°$ and distance to the LMC greater than $10°$ are used. Blue filled circles show the locations of two known objects in the field of view: Pictor II and KMHK 1762. In this part of the sky, there are also several star clusters: NGC 2808, IC 4499, and E3. However, these are detected with significance in excess of 20 and are omitted in the plot. Other detected overdensities are shown as black points, the new discoveries, Car II and III are shown as red filled circles. There are also a small number of detections associated with data artefacts that are shown in light grey. The red dashed line marks the $S_{\mathrm{L}} = 6$ threshold. Objects with high S but low S_{L} are likely associated with areas in which the variance was underestimated. The region above the red line offers a clean candidate selection.

old and metal poor population at the distance of 35 kpc and $r > 21$. The map highlights the almost continuous MagLiteS coverage of the area and the stability of its photometry. Note that the $r > 21$ cut is just to select MSTO stars, and do not represent the limiting magnitude of MagLiteS, which is closer to ∼23 mag. The outskirts of the LMC's disc are clearly visible, extending beyond 10 deg from the Cloud's centre. In fact, a diffuse stellar cloud associated with the LMC can be seen stretching as far as ∼15 deg and engulfing the recently discovered Pictor II (Pic II; Drlica-Wagner et al. 2016a). Carina II and III stand out dramatically in the density map at an angular separation of ∼18 deg from the LMC. As this figure demonstrates, the Carinas are ∼17 deg from the Galactic plane. Despite the close proximity to the Galactic disc, the extinction is low and therefore does not seem to affect the stellar distribution significantly.

The right panel of Fig. 2 presents the colour–magnitude diagram (CMD) of stars centred on Carina II. The portion of the CMD with $r < 20$ is dominated by the Galactic disc dwarfs (unsurprisingly, given the low Galactic latitude of the object), thus concealing the object's Red Giant Branch (RGB). Nonetheless, the pile-up of stars around the satellite's turn-off is visible at $(g - r)_0 \sim 0.4$ and $r_0 \sim 21.5$. Even more obvious are the Blue Horizontal Branch (BHB) stars at $(g - r)_0 < 0$ and $r \sim 18.5$. Additionally, right under the BHB, a sprinkle of stars that looks like Blue Straggler can be seen at $(g - r)_0 < 0$ and $r \sim 21$.
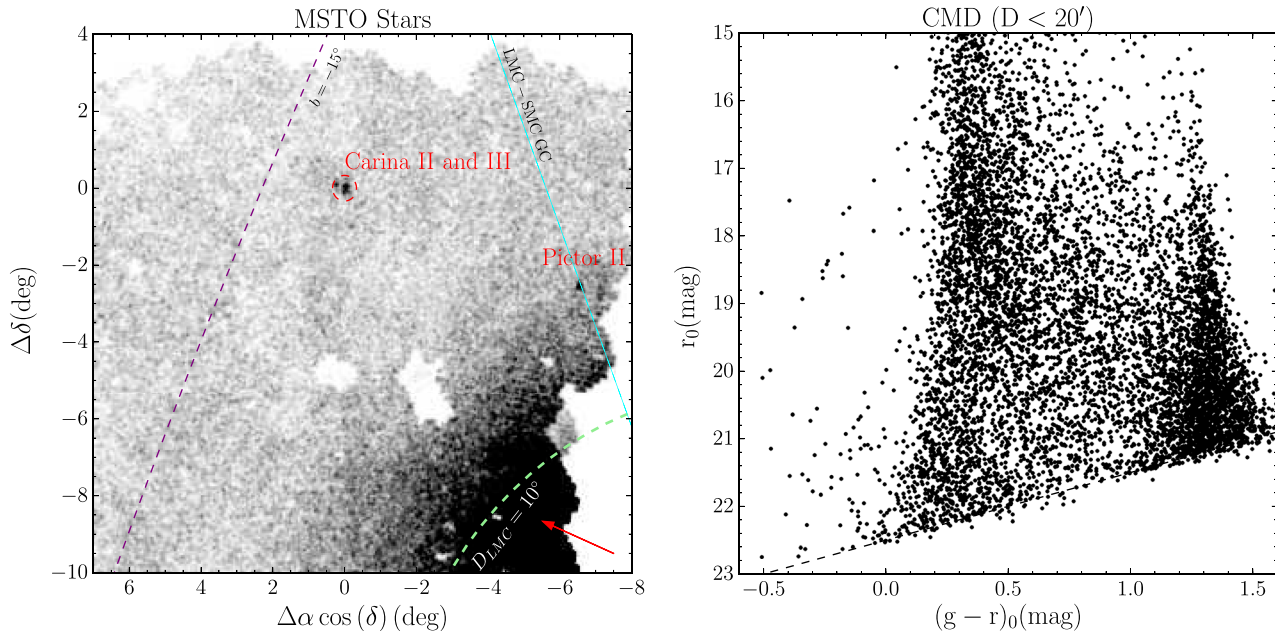
Figure 2. Distribution of stars in the area around Carina II and III in the MagLiteS survey data. Left: Spatial distribution of the MSTO stars at ∼35 kpc, where an overdense region corresponding to Car II and III can be easily seen near the centre of the figure. The compact overdensity near the right edge of the panel is the Pic II satellite. The constant Galactic latitude line ($b = -15°$) is shown in purple, a circle with $10°$ radius centred on the LMC is shown as a dashed green line. The Cloud's proper motion vector shown as a red arrow. The line connecting the LMC and SMC is shown in cyan. Right: CMD of the stars within 20 arcmin of the centre of the Carinas. A sequence of BHB stars is clearly visible at $r \sim 18.5$ as well as hints of a corresponding MSTO at $r \sim 21.5$.

3 FOLLOW-UP IMAGING

In addition to the original MagLiteS data, two series of follow-up DECam imaging were obtained of the Carina II+III field during Blanco 4m Director's Discretionary and engineering time on the nights of 2017 January 17 and February 12, both of them with bright moon. During each of those two nights the Carinas were observed multiple times in *gri* over a period of ∼7 h. Several *u*-band exposures were also taken during the periods of time on those nights when the Moon was below the horizon. In addition, several *gri* exposures were obtained on each of 2017 February 9–11. In total, we obtained 42 epochs in *u* and 70 epochs in each *gri*. Exposure times were 120s in *u* and 60s in *gri*. Both galaxies were covered by a single DECam field. The observing sequence consisted of a [*u*]*gri* of a field in which Carina II was centred on one of the central CCDs of the camera (N4), followed immediately by another sequence with offsets in RA and DEC of 60 arcsec to cover the gaps between CCDs.

These individual exposures were processed with software equivalent to the standard DES processing pipeline. The astrometric residuals are ∼40 mas rms and the photometric calibration has an accuracy of 2 per cent rms in *gri* and 5 per cent in *u*. Objects were detected using standard SExtractor (a simple cut on |spread_model| < 0.003 was used to separate stars from extended objects and objects with SExtractor flags <4 were kept allowing close blends in this relatively crowded field at $(l, b) = (270 \deg, -17 \deg)$. Individual exposure and filter catalogues were matched using the *STILTS* software package[2] (Taylor 2006). This yielded ugri light curves with up to 70 epochs for over 30 000 objects within 0.6 deg of the centre of Carina II+III. RR Lyrae stars associated with Carina II were

identified as described below and used to refine the distance to the Carina II system, along with a number of field eclipsing binaries.

In addition to the light-curve data, deep coadds were constructed from all of the available imaging data. Catalogues from these coadds were extracted and resulted in detection limits approximately half a magnitude deeper in *g* and *r* bands ($r \sim 23.5$) than the discovery MagLiteS exposures themselves.

3.1 RR Lyrae stars

To search for variable stars we used the time series data in *gri* only because the *u* data does not have an extended time baseline. We flagged stars as variable if the standard deviation of their magnitudes in each band is 3σ above the distribution for the bulk of the population (which is non-variable) of similar magnitude. In order to avoid spurious variables, we required that the stars were flagged as variable in all three bands. The amplitude of variation of RR Lyrae stars is large enough in all optical bands that there is no risk of missing one due to this requirement. This selection results in 167 variable stars (0.7 per cent of the total) for further study.

The selected variable stars were then searched for periodicity using an implementation of the well known Lafler & Kinman (1965) algorithm that uses the information in all three bands simultaneously (see Vivas et al. 2016). We searched for RR Lyrae stars in the range 0.2–0.9 d, and for SX Phe/δ Scuti stars in the range 0.01–0.2 d. In total we found 51 periodic variable stars in the field, 5 of which we classified as RR Lyrae stars. The remaining 46 stars were different types of eclipsing systems (see Appendix). No short period variables exemplifying the SX Phe or δ Scuti stars were found. On the other hand, our cadence is not sensitive to periods larger than 1 d and hence, the Anomalous Cepheid stars range was not fully explored. Nevertheless, we looked at the time series of all variable stars candidates in the region of the CMD where Anomalous

---

[2] http://www.star.bris.ac.uk/~mbt/stilts
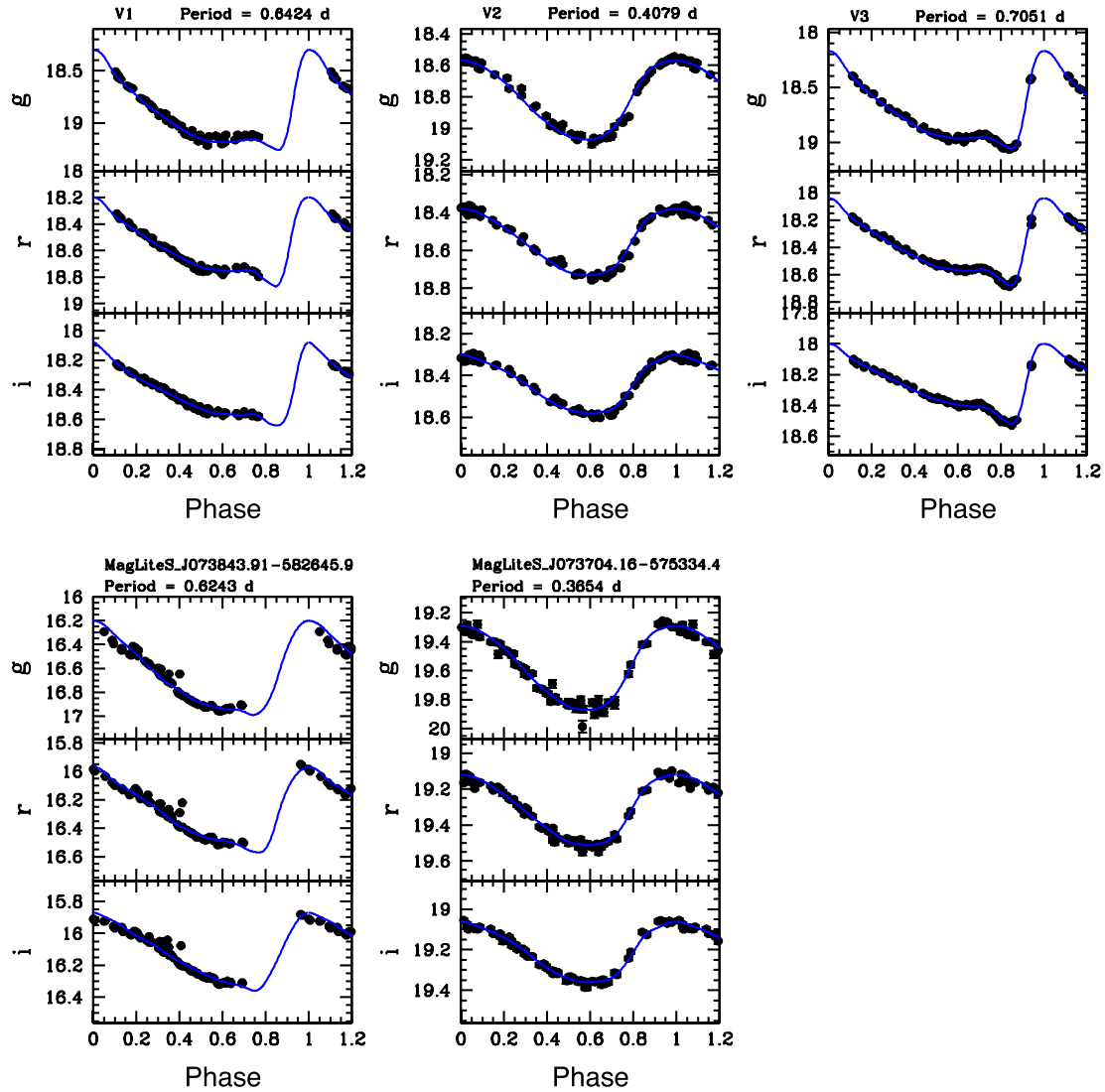
Figure 3. Light curves of the 5 RR Lyrae stars – two RRc stars (middle panels) and three RRab stars – found within 0.6 deg from the centre of Carina II. The three stars in the top row (CarII-V1 to CarII-V3) have mean magnitudes and location consistent with being members of Carina II. The two stars in the bottom row are halo stars along the line of sight, although MagLiteS_J073704.16-575334.4, located at ∼48 kpc might be associated with the LMC. The solid blue lines are templates fitted to the data from the library of Sesar et al. (2010).

Table 1. Coordinates, period, amplitudes, mean magnitudes in *gri*, and distance for the 5 RR Lyrae stars in the DECam field.

ID	RA (deg)	DEC (deg)	Type	Period (d)	Δ_g (mag)	g (mag)	Δ_r (mag)	r (mag)	Δ_i (mag)	i (mag)	d_{Car2} (′)	d_H (kpc)	Var
MagLiteS_J073637.00-580114.4	114.15416	−58.02068	ab	0.6424	0.96	18.88	0.67	18.57	0.56	18.42	2.1	38.1 ± 0.4	CarII-V1
MagLiteS_J073704.16-575334.4	114.26732	−57.89288	c	0.3654	0.58	19.56	0.39	19.31	0.30	19.21	7.3	47.6 ± 0.6	
MagLiteS_J073645.85-575154.1	114.19105	−57.86502	c	0.4079	0.50	18.81	0.35	18.55	0.28	18.44	7.7	37.3 ± 0.4	CarII-V2
MagLiteS_J073509.12-575714.8	113.78799	−57.95410	ab	0.7051	0.89	18.70	0.64	18.39	0.52	18.27	10.9	36.7 ± 0.4	CarII-V3
MagLiteS_J073843.91-582645.9	114.68295	−58.44607	ab	0.6243	0.79	16.62	0.60	16.28	0.49	16.12	32.6	12.0 ± 0.1	

Cepheid are located, searching for smooth variations in time-scales >1.0 d, and found none. Light curves in *gri* for the five RR Lyrae stars (three of type ab and two of type c) found in the field are shown in Fig. 3.

We obtained mean magnitudes of the RR Lyrae stars by fitting templates from the library by Sesar et al. (2010), which is based on

RR Lyrae stars in SDSS Stripe 82. The light curves were integrated in intensity units and the mean value transformed back to magnitudes. By using a template we overcome any possible bias in the mean magnitude due to uneven sampling of the light curve, as is the case for several of our stars (Fig. 3). In Table 1, we provide coordinates, periods, amplitudes, and mean magnitudes in each band
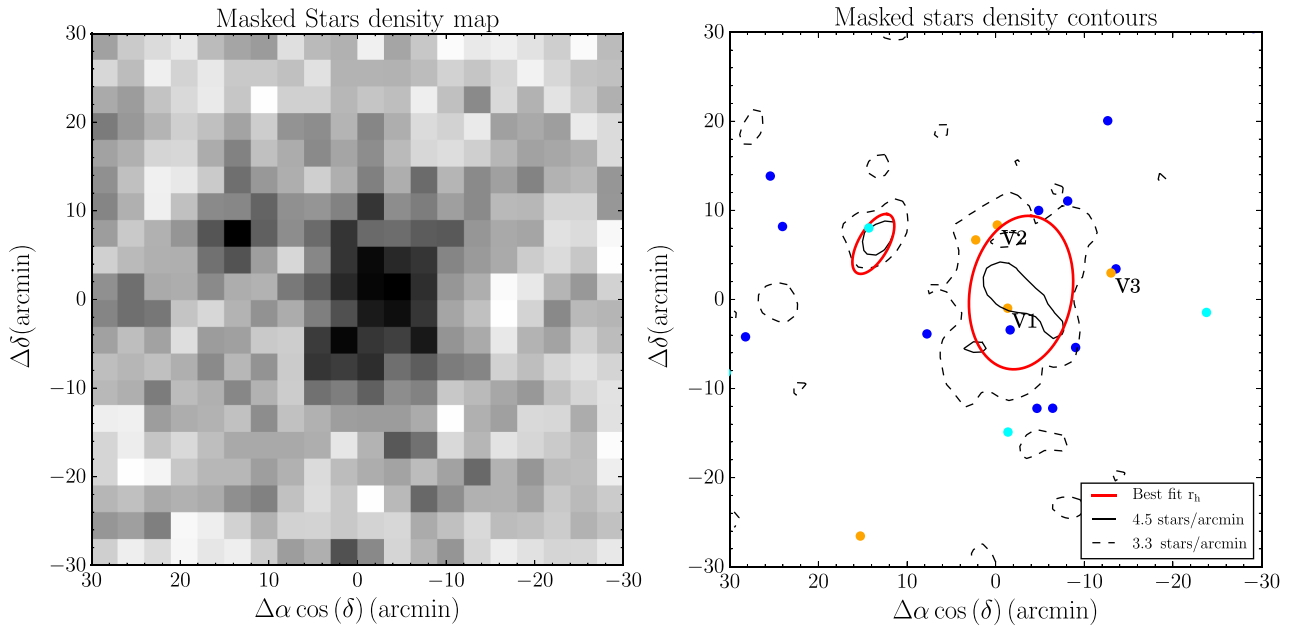
Figure 4. Deep follow-up imaging of the Carina satellites Left: Density map of stars within a CMD mask defined by the best-fitting isochrone of Carina II. Right: Density contours of the same region of the sky with the half-light radius of the best-fitting models overplotted in red. Stars within 0.3 mag from the BHB ridge line of Car II(III) are shown in blue(cyan), and RR Lyrae stars found in the field are shown in orange. Both overdensities are clearly seen in the density maps and are well reproduced by the models.

for the RR Lyrae stars. The last three columns in Table 1 contain the separation in the sky (in arcmin) from the centre of Carina II, the heliocentric distance which was calculated as described in Section 3.2, and a variable designation (CarII-V1 to CarII-V3) for the stars which are members of Carina II.

From the spatial distribution of the RR Lyrae stars in the region (see Fig. 4) it is clear that all but one of the RR Lyrae stars are close enough, <11 arcmin, to the centre of Carina II to suspect a relationship. However, the location of these stars in the CMD (Fig. 5) confirms that only three of them (MagLiteS_J073637.00-580114.4, MagLiteS_J073645.85-575154.1, and MagLiteS_J073509.12-575714.8) are at the level of the horizontal branch of Carina II. These stars were designated as CarII-V1 to CarII-V3. Stars CarII-V1 and CarII-V2 were recently confirmed as members of Carina II based on their radial velocities (Li et al., in preparation). No spectroscopic observations for CarII-V3 are yet available.

Star MagLiteS_J073704.16-575334.4 is at only 7.3 arcmin from the centre of Carina II but it is ∼0.8 mag fainter than the other three stars. Thus, this star, as well as MagLiteS_J073843.91-582645.9, which is ∼33 arcmin from the centre of Carina II and ∼2 mags brighter than its HB, are not associated with either of the Carinas.

None of the RR Lyrae stars are located near Carina III. If Carina III is confirmed as a UFD (rather than a stellar cluster), this would be the first of all satellite galaxies – that have been searched for variable stars – in which no RR Lyrae stars have been found (see compilations in Baker & Willman 2015; Vivas et al. 2016).

3.2 Distance to Carina II from RR Lyrae Stars

To calculate the heliocentric distances to the RR Lyrae stars, we used the relationships for the absolute magnitude in the SDSS-i-band (i_S, where the subscript S stands for SDSS), M_i, provided by Cáceres & Catelan (2008), which are based on theoretical models

of these stars in the SDSS bands, and depend on both the period and the metallicity for the star. Since our magnitudes are tied to the DES (AB) photometric system, we first transformed our i mean magnitudes to i_S using

$$i = i_S + 0.014 - 0.214\,(i-z)_S - 0.096\,(i-z)_S^2.$$
$$z = z_S + 0.022 - 0.068\,(i-z)_S \qquad (2)$$

These transformation equations contain a colour term with $(i-z)$, which we do not have in our time series observations. Because RR Lyrae stars have very small dispersion in the mean $(i-z)$ colour distribution (Vivas et al. 2017), we used the mean colour of the RR Lyrae stars in the globular cluster M5 $((i-z)_0 = 0.013$ and -0.006, for ab and c-type, respectively) as provided in Vivas et al. (2017). For the stars suspected to be members of Carina II, we assumed a metallicity of [Fe/H] $= -2.4$ based on the spectroscopy recently obtained by Li et al. (in preparation) for this galaxy. We also assumed [α/Fe] $= 0.2$, which is typical of ultra-faint galaxies (Pritzl, Venn & Irwin 2005). For the two suspected halo stars, we assumed [Fe/H] $= -1.65$ and [α/Fe] $= 0.3$. Individual heliocentric distances are provided in Table 1.

Thus, the distance to Carina II based on its three RR Lyrae stars is 37.4 ± 0.4 kpc, in agreement with the structural parameters derived from the CMD fitting described in the next section. Star MagLiteS_J073843.91-582645.9 is a foreground halo star at 12.0 ± 0.1 kpc from the Sun, while MagLiteS_J073704.16-575334.4 is behind Carina II, at 47.6 ± 0.6 kpc. The latter is located exactly at the distance at which material from the LMC would be expected (Muñoz et al. 2006). Spectroscopy will be needed to confirm if this distant RR Lyrae star is indeed associated with the LMC.

3.3 Properties of the Carina II RR Lyrae stars

The pulsational properties of RR Lyrae stars in satellite galaxies are useful to understand the role of these systems in the formation
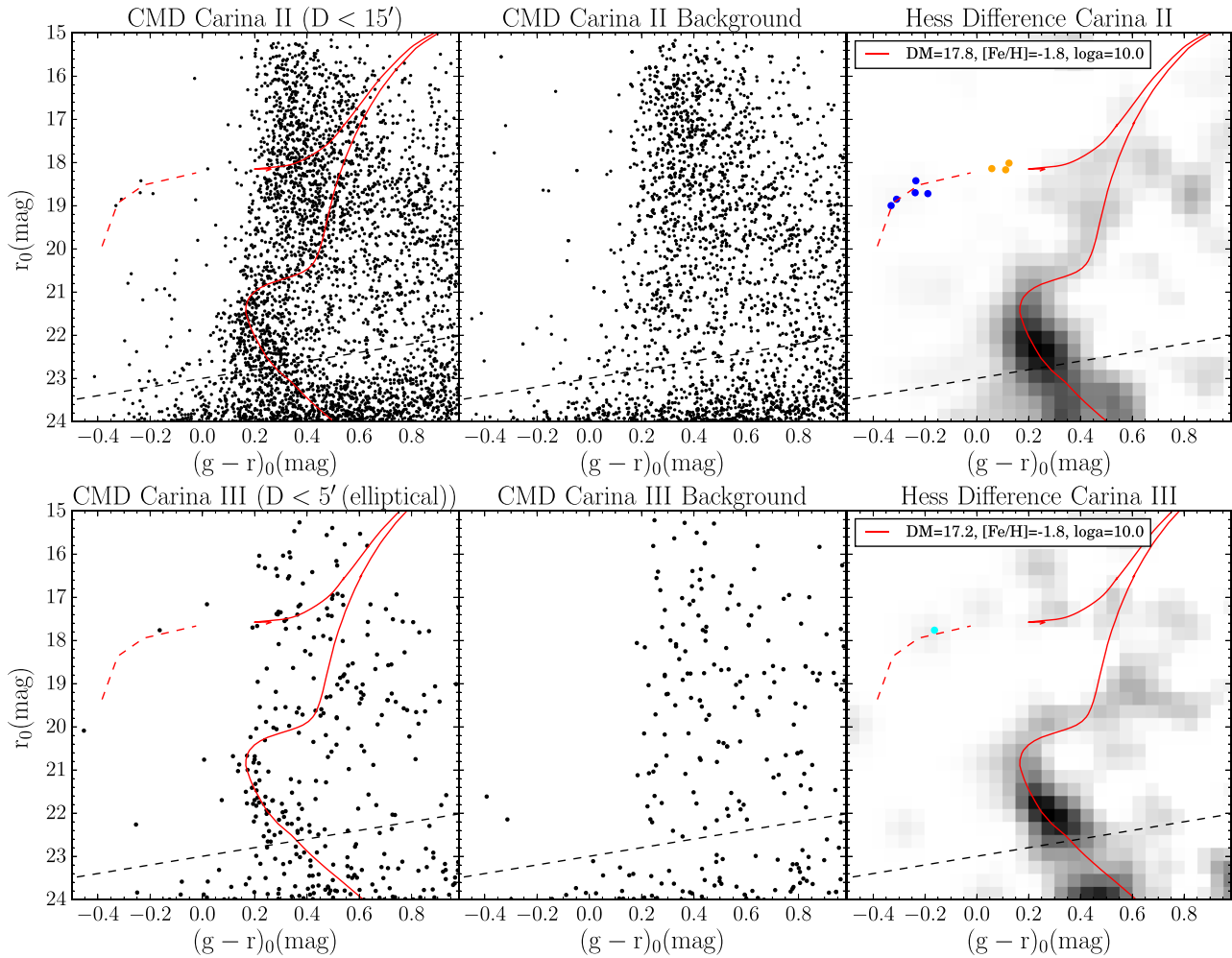
Figure 5. CMD and Hess difference diagram for the Carina II and III systems. Top (bottom) row presents CMD information for Carina II (Carina III). Left-hand panel gives the CMD within twice the half-light radius of the satellite, middle panel shows the CMD of the foreground stellar population estimated for the same solid angle as used for the left-hand panel. Finally, right-hand panel demonstrates the foreground subtracted Hess difference diagram. Solid red line shows the best-fitting isochrone (see Section 4 for details), while the red dashed line indicates the M92 BHB ridge-line shifted to the distance of each satellite. In blue (cyan), we identify individual BHB candidates for Carina II (III), and in orange we show RR Lyrae stars identified at the same distance as Carina II. Note that the neither the BHB stars nor the RR Lyrae stars were used in the determination of the best isochrone and therefore provide an independent confirmation of the distance. For both Carina II and III, the Hess difference diagrams and the CMDs clearly show prominent MSTO features that are absent in the foreground thus confirming that Carinas are geniune stellar systems in the Milky Way halo. The black dashed line is the $g, r = 23$ magnitude limit used in the modelling.

of large galaxies like the Milky Way (Clementini 2014; Zinn et al. 2014; Fiorentino et al. 2015; Vivas et al. 2016). In particular, the mean period of the fundamental mode RR Lyrae stars (ab-type) can be used to classify the stellar system in Oosterhof (Oo) groups (Oosterhoff 1939; Catelan & Smith 2015). With only a couple of exceptions (Canes Venatici I and Ursa Major I, Clementini 2014) that belong to an intermediate Oo group, all other ultra-faint dwarf (UFD) galaxies have been classified as Oo II (see compilation in Vivas et al. 2016). Carina II follows that trend. Although it has only 2 ab-type RR Lyrae, their mean period is 0.67d, close to the nominal 0.65d of the OoII group (Catelan & Smith 2015).

With 3 RR Lyrae stars, Carina II resembles Leo V, a UFD with similar absolute magnitude, $M_V = -4.4$, and containing also three RR Lyrae stars (Medina et al., in preparation). Ursa Major II and Canes Venatici II which also have similar brightness, $M_V = -4.0$ and -4.6, respectively (Sand et al. 2012), have one and two RR

Lyrae stars (Dall'Ora et al. 2012; Greco et al. 2008). Thus, the production of RR Lyrae stars in Carina II follows the trend of galaxies of similar brightness in the Milky Way system.

4 STRUCTURAL PARAMETERS

We measure the properties of Carina II and III by modelling the magnitudes, colours, and positions of stars extracted from the deep co-added images (see above) in an area ~ 1 deg $\times$ 1 deg centred on Car II (see e.g. Martin, de Jong & Rix 2008; Koposov et al. 2015; Torrealba et al. 2016b, for a similar approach). To avoid density variations caused by spatially varying incompleteness as well as to avoid the contamination due to misclassified galaxies, we only consider stars brighter than 23 in g and r. We also correct for extinction using the Schlegel et al. (1998) maps, but used updated coefficients for the DES filters, namely, $A_g/E(B - V) = 3.184$ and

$A_r/E(B - V) = 2.13$. Additionally, given the close proximity of the two satellites to each other, we model their stellar components simultaneously. Therefore, our model probability density function (PDF) describing the positions, colours, and magnitudes of the stellar data has three components, namely, the background plus the two satellites:

$$P(\Phi|\Theta) = \prod_i \left(f_1 P_s(\Phi_i|\Theta_1) + f_2 P_s(\Phi_i|\Theta_2) + f_b P_b(\Phi_i|\Theta_b) \right), \quad (3)$$

where the product is over all stars within the modelled area. $\Phi = (x, y, g - r, r)$ is a shorthand for the observed properties of the stars, namely, the on sky positions (x, y), their colours $(g - r)$, and magnitudes r. f_1 is the fraction of stars in Car II, f_2 the fraction of stars in Car III, and $f_b = 1 - f_1 - f_2$ the fraction of stars in the background. Θ stands for all of the model parameters, which are divided between the three components using the same sub-indexes as the fractions f.

For each satellite, the PDF, $P_s(\Phi|\Theta_k)$ is composed of the spatial model, $P_{sp}(x, y|\Theta_{k,sp})$, and the colour–magnitude model, $P_{cmd}(g - r, r|\Theta_{k,cmd})$. The spatial model for the Carinas is defined as a two-dimensional elliptical Plummer sphere:

$$P_{sp}(x, y|\Theta_{k,s}) = \frac{1}{\pi a^2 (1 - e)} \left(1 + \frac{\tilde{r}^2}{a^2} \right)^{-2}, \quad (4)$$

where $\tilde{r}^2 = \tilde{x}^2 + \tilde{y}^2$ is the elliptical radius and

$$\begin{bmatrix} \tilde{x} \\ \tilde{y} \end{bmatrix} = \begin{bmatrix} \cos\theta/(1-e) & \sin\theta/00(1-e) \\ -\sin\theta & \cos\theta \end{bmatrix} \begin{bmatrix} x - x_0 \\ y - y_0 \end{bmatrix},$$

where the five parameters of the spatial model are: the centre of the Plummer profile (x_0, y_0), the elliptical half-light radius a, the ellipticity e, and the positional angle of the major axis θ.

The PDF in colour–magnitude space, P_{cmd}, is defined using PARSEC isochrones (Bressan et al. 2012) populated according to the Chabrier (2003) stellar mass function. Specifically, this PDF is constructed on a pixel grid in the $(g - r, r)$ space and the probabilities of finding a star in each bin given an isochrone are found by convolving the expected number of stars along the isochrone track with the corresponding photometric errors. This probability distribution depends on three parameters: the isochrone age, metallicity, and the distance modulus. One should be aware, however, that this approach comes with several limitations. In particular, the uncertainties in the modelling of the isochrones, which can give rise to systematic errors (see e.g. Drlica-Wagner et al. 2016a) are not considered. Also, the PARSEC isochrones only have metallicities down to -2.1 dex (Bressan et al. 2012), and hence the presented approach cannot account for metallicities lower than this limit. Furthermore, the differences between isochrones become smaller at decreasing metallicities, making it more difficult to distinguish different metallicities at the low-metallicity end. This issue is of particular importance for faint satellites – like the ones presented in this paper – since the main effect of the metallicity to the shape of the isochrone, at fixed age an distance, is to shift the RGB, which is poorly populated in these objects.[3]

The PDF for the stellar foreground/background population is also defined as the product of the spatial component and a colour–magnitude component: $P_b(\Phi|\Theta_{bg}) = P_{bg,sp}(x, y|N_{bg}, b_1,$

Table 2. Properties of Car II and Car III.

Property	Carina II	Carina III	Unit
α(J2000)	114.1066 ± 0.0070	114.6298 ± 0.0060	deg
δ(J2000)	-57.9991 ± 0.0100	-57.8997 ± 0.0080	deg
$(m - M)$	17.79 ± 0.05	17.22 ± 0.10	mag
$D_\odot$	36.2 ± 0.6	27.8 ± 0.6	kpc
r_h	8.69 ± 0.75	3.75 ± 1.00	arcmin
r_h	91 ± 8	30 ± 9	pc
$1-b/a$	0.34 ± 0.07	0.55 ± 0.18	
PA	170 ± 9	150 ± 14	deg
M_V	-4.5 ± 0.1	-2.4 ± 0.2	mag
[Fe/H]	-1.8 ± 0.1	-1.8 ± 0.2	dex
Age	9.9 ± 0.4	9.7 ± 0.8	Gyr

$b_2)P_{bg, cmd}(g - r, r)$. The spatial model for the background is defined as a bilinear distribution of the form:

$$P_{bg,sp}(x, y|N_{bg}, b_1, b_2) = \frac{1}{N_{bg}}(b_1 x + b_2 y + 1), \quad (5)$$

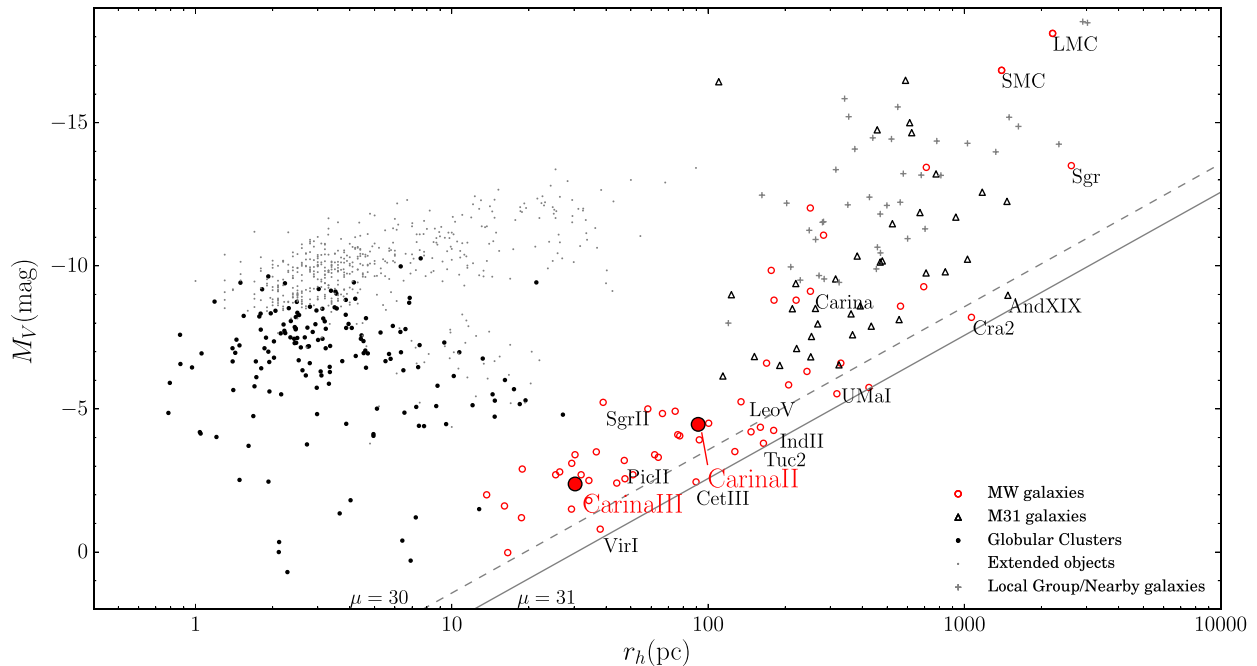where b_1 and b_2 define the two-dimensional background gradient, and N_{bg} is defined so $P_{bg, sp}$ is normalized to one over the modelled area. The colour–magnitude component of the background does not have any extra parameters, since it is defined empirically by constructing a histogram in colour–magnitude space using the stars outside 20 arcmin from the centre of Car II, and normalized to unity.

The full model contains 20 free parameters, 2 for the background and 9 for each of the satellites. We sample the likelihood with the affine invariant ensemble sampler (Goodman & Weare 2010) implemented in the EMCEE python module (Foreman-Mackey et al. 2013). We use flat priors over all the parameters except the spatial size parameter, a, of both satellites, for which we use the uninformative Jeffreys prior $P(a) \propto \frac{1}{a}$. We measure the best-fitting parameters and their uncertainties from the marginalized posterior distributions as the 15.9 per cent, 50 per cent, and 84.1 per cent percentiles. The values of the key parameters with their uncertainties are given in Table 2. Note that since the errors in this case are symmetric, we report the average between the 15.9 per cent and 84.1 per cent percentiles in the table.

Car II is best fit by a mildly elliptical profile with $e = 0.34 \pm 0.07$ and an elliptical half-light radius of $r_h = 8.7 \pm 0.8$, while Car III is much smaller at $r_h = 3.75 \pm 1$. It also appears to be significantly elongated with $e = 0.55 \pm 0.18$. The best-fitting spatial models are shown in Fig. 4. The left-hand panel of the Figure shows the density map of the stars inside a mask created using the best-fitting isochrone of Car II. We note that while this mask is not ideal for showing Car III, due to differences between the isochrones of Car II and Car III, the overlap between the two populations is large enough to reveal both overdensities on the map. In the right-hand panel, we show stellar density contours together with the half-light ellipses of the best-fitting models. We also show the BHB candidates selected within 0.3 magnitudes from the BHB ridge-line of Car II (III) in blue (cyan) and the RR Lyrae stars in orange. It is remarkable that BHB stars appear to be distributed more diffusely than the bulk of the other stellar populations (such as RGB and MSTO). Note that the spread out appearance of the BHB candidate stars, together with the elongation of both satellites in the same direction might indicate tidal disruption.

The final confirmation of the genuine nature of the Car II and III system is given in Fig. 5, where we show the CMD and Hess difference diagrams for each object. Panels in the left column show the

---

[3] Note that, at fixed age and distance, the difference between the tip of the RGB gets as small as 0.02 in $g - r$ and less than 0.1 magnitudes in r between the two lower metallicity isochrones.

Figure 6. Absolute magnitude versus half-light radius for stellar systems in the Local Group. Local galaxies from McConnachie (2012) (updated 2015 September): dwarf galaxy satellites of the Milky Way are shown with red open circles, the M31 dwarfs with black unfilled triangles, and other nearby galaxies with grey crosses. The positions of Crater 2 (Torrealba et al. 2016a), Aquarius 2 (Torrealba et al. 2016b), DESJ0225+0304 (Luque et al. 2017), Pic II (Drlica-Wagner et al. 2016b), Virgo I (Homma et al. 2016), and Cetus III (Homma et al. 2017) are also displayed. Black dots are the Milky Way globular clusters measurements (from Belokurov et al. 2010; Harris 2010; Muñoz et al. 2012; Balbinot et al. 2013; Kim & Jerjen 2015a; Kim et al. 2015, 2016; Laevens et al. 2015; Luque et al. 2016, 2017; Martin et al. 2016; Weisz et al. 2016; Koposov, Belokurov & Torrealba 2017) and grey dots are the extended objects smaller than 100 pc from Brodie et al. (2011). The black solid (dashed) line corresponds to the constant (effective) surface brightness (i.e that within half-light radius) of $\mu = 31$ (30) mag arcsec^{-2}. The surface brightness limit of the searches for resolved stellar systems in the SDSS (Koposov et al. 2008) and similar surveys is $\lesssim 30$ mag arcsec^{-2}.

CMDs within 15 arcmin for Car II and 5 arcmin for Car III, while the middle panels give the CMDs of the foreground stars from a region of the same area but at least 30 arcmin away from the centre of each satellite. Finally, the right panels present the foreground subtracted Hess difference diagrams. The shapes of the spatial regions that define the Hess difference diagram as well as the isochrones (shown in red lines) are dictated by the best-fitting models described above. The blue (cyan) points show BHB candidates for Car II (Car III), and the red dashed line is the M92 BHB ridge-line shifted to the distance of the isochrone. Note that the BHBs present in both satellites are not considered in either the modelling or the search, and therefore provide independent confirmation of Car II and III and their distance estimations. Both satellites have a clear MSTO – where very little background is expected, as shown by the background CMD – and are well described by the best-fitting isochrones. As evident from the CMDs and the model isochrones, CarII and III clearly possess distinct stellar populations. Specifically, while both stellar population are consistent with an old (∼10 Gyr) and metal poor ([Fe/H] = −1.8 ± 0.1) populations, Car II has a distance modulus of 17.79 ± 0.05, placing it at ∼36.2 ± 0.6 kpc, but Car III, on the other hand, has a distance modulus of 17.22 ± 0.10, which is equivalent to a distance of ∼27.8 ± 0.6 kpc.

Finally, we also measure the luminosity of the two newly discovered satellites. The number of stars with $g, r < 23$ from the best-fitting model is 709 ± 58 and 156 ± 32 in Car II and Car III, respectively. Combining the best-fitting isochrones with a Chabrier initial mass function, we can estimate the absolute luminosity of each object. We measure $M_V = -4.5 \pm 0.1$ for Car II and $M_V = -2.4 \pm 0.2$

for Car III, confirming that Car III is ∼7 times fainter than its neighbour.

5 DISCUSSION AND CONCLUSIONS

MagLiteS has explored uncharted regions of the sky in pursuit of an entourage of smaller satellites of the Magellanic Clouds. Using this data set, we have discovered two new ultra-faint satellites in the vicinity of the LMC. Named after the constellation in which they are located, Carina II and III are separated by only a few arcminutes, making them a tight pair on the sky. Analysis of their stellar populations, supported by the presence of prominent MSTO features, reveals that they are relatively close to each other physically (separated by ∼10 kpc), but perhaps more interesting is that they are only ∼20 kpc from the LMC. Whether this association, with the LMC and between the Carinas, is physical or circumstantial is key to revealing their origin, and could be an important ingredient in measuring the properties of the LMC itself and the role of its satellites in the Milky Way halo.

Fig. 6 shows Car II and III in the context of the structural properties of the satellite population of the Milky Way. Both satellites lie in a region of size–luminosity space occupied by the ultra-faint dwarfs, close to the detection limit of current surveys. It should be noted that signs of tidal disruption, as hinted by the highly elliptical profile of Car III, and a diffuse population of BHB candidates present in the case of Car II, could lead to mildly inflated size measurements. Even in this scenario, both Carinas appears to be much too diffuse to be globular clusters, although for Car III, its smaller
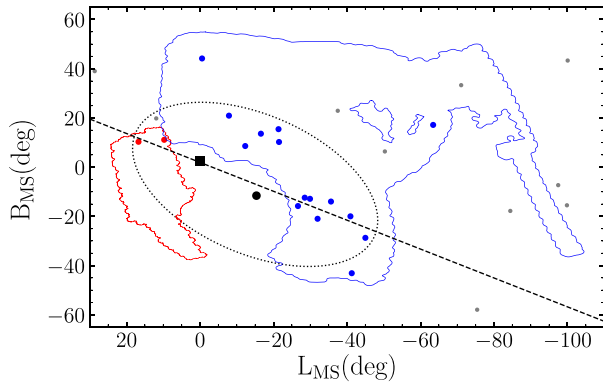
Figure 7. On-sky positions of satellites within 300 kpc from DES (blue), MagLites (red, note Car II and III are merged into a single point), the LMC (black square), and SMC (black circle) shown in Magellanic Stream coordinates (Nidever, Majewski & Butler Burton 2008). Other satellites in the region are shown in grey. We also show the footprints of DES/MagLiteS in blue/red. The dashed line is the best-fitting line to the positions of the MagLites satellites, Magellanic Clouds, and the 7 DES satellites with $B_{MS} < 0$. The dotted ellipse represents an alternative, broader model distribution.

physical size may actually be consistent with the hypothesis of a disrupting globular cluster. Despite the strong structural evidence for Car II, the robust determination as to whether Car II and Car III are indeed dwarf galaxies or extended/tidally disrupting globular clusters can only be decided through the analysis of the kinematics and/or metallicities of their stellar members (see Li et al., in preparation, for a spectroscopic analysis).

5.1 Anisotropy in the DES/MagLiteS satellite distribution

The distribution of satellites discovered in DES is highly anisotropic. DES satellites preferentially lie towards the southern edge of the survey, bordering the Magellanic Clouds, providing some evidence for a physical association between these groups (Drlica-Wagner et al. 2015; Koposov et al. 2015). Fig. 7 hints at a further anisotropy in the distribution of dwarf galaxies in the vicinity of the Magellanic Clouds. It shows the positions of all dwarfs and dwarf candidates within 300 kpc discovered in DES (blue circles) and MagLiteS (red circles). Other satellites in the region are displayed as grey circles. All three MagLiteS discoveries are well aligned with the line connecting the LMC and SMC. Additionally, seven of the DES discoveries seem to fall along the same tight linear sequence on the sky. We add to Fig. 7 the best-fitting line to this subset of the DES satellites, the MagLiteS satellites, and the Magellanic Clouds. This line passes through the position of the LMC, while the standard deviation of vertical distance of the sample from this line is only 3 deg. This elongation of the observed satellite distribution along the LMC–SMC separation vector is an interesting curiosity. Hydra II, which has been associated with the LMC leading arm (Martin et al. 2015), sits at the opposite direction of the planar anisotropy traced by the DES and MagLiteS dwarfs.

What could the nature of this anisotropy be? An on-sky linear alignment could, of course, correspond to a 3D planar structure. Prior to any MagLiteS discoveries, J16 considered the group of seven DES satellites with negative B_{MS}, finding that they lie in a plane with rms thickness 2.7 kpc, which also contained both the LMC and SMC. Pic II, Car II, and Car III have distances from the plane, as defined in that work, of 2.0 kpc (Drlica-Wagner et al. 2016a), 1.8 kpc, and 1.0 kpc, respectively, i.e. all less than the orig-

inally quoted rms thickness of the plane. This may suggest that the Carinas, Pic II and half of the DES satellites may comprise a *Magellanic satellite plane*, though such a conclusion is highly speculative. When *all* of the DES and MagLiteS satellites are considered together their distribution may just be described by a broad ellipse, elongated in the direction of the line connecting LMC and SMC (e.g. the dotted ellipse in Fig. 7), rather than a thin plane. For now, we simply note this interesting feature in the observed distribution, but defer quantitative analysis of the exact nature of this anisotropy to a future work.

REFERENCES

Baker M., Willman B., 2015, AJ, 150, 160
Balbinot E. et al., 2013, ApJ, 767, 101
Bechtol K. et al., 2015, ApJ, 807, 50
Belokurov V., 2013, New Astron. Rev, 57, 100
Belokurov V. et al., 2010, ApJ, 712, L103
Bertin E., 2006, in Gabriel C., Arviset C., Ponz D., Enrique S., eds., ASP Conf. Ser. Vol. 351, Astronomical Data Analysis Software and Systems XV. Astron. Soc. Pac., San Francisco, p. 112
Bertin E., 2011, in Evans I. N., Accomazzi A., Mink D. J., Rots A. H., eds., ASP Conf. Ser. Vol. 442, Astronomical Data Analysis Software and Systems XX. Astron. Soc. Pac., San Francisco, p. 435
Bertin E., Arnouts S., 1996, A&AS, 117, 393
Bressan A., Marigo P., Girardi L., Salasnich B., Dal Cero C., Rubele S., Nanni A., 2012, MNRAS, 427, 127
Brodie J. P., Romanowsky A. J., Strader J., Forbes D. A., 2011, AJ, 142, 199
Cáceres C., Catelan M., 2008, ApJS, 179, 242
Cannon R. D., Hawarden T. G., Tritton S. B., 1977, MNRAS, 180, 81P
Catelan M., Smith H. A., 2015, Pulsating Stars. Wiley, New York
Chabrier G., 2003, PASP, 115, 763
Clementini G., 2014, in Guzik J. A., Chaplin W. J., Handler G., Pigulski A., eds., Proc. IAU Symp. 301, Precision Asteroseismology. Cambridge Univ. Press, Cambridge, p. 129
D'Onghia E., Lake G., 2008, ApJ, 686, L61
Dall'Ora M. et al., 2012, ApJ, 752, 42
Deason A. J., Wetzel A. R., Garrison-Kimmel S., Belokurov V., 2015, MNRAS, 453, 3568
DES Collaboration, 2005, preprint (arXiv:astro-ph/0510346)
Drlica-Wagner A. et al., 2015, ApJ, 813, 109
Drlica-Wagner A. et al., 2016a, ApJ, 833, L5
Drlica-Wagner A. et al., 2016b, ApJ, 833, L5
Fiorentino G. et al., 2015, ApJ, 798, L12
Flaugher B. et al., 2015, AJ, 150, 150
Foreman-Mackey D., Hogg D. W., Lang D., Goodman J., 2013, PASP, 125, 306
Gómez F. A., Besla G., Carpintero D. D., Villalobos Á., O'Shea B. W., Bell E. F., 2015, ApJ, 802, 128
Goodman J., Weare J., 2010, Comm. App. Math. Comp. Sci, 5, 65
Greco C. et al., 2008, ApJ, 675, L73
Harris W. E., 2010, preprint (arXiv:1012.3224)
Homma D. et al., 2016, ApJ, 832, 21
Homma D. et al., 2017, preprint (arXiv:1704.05977)
Jethwa P., Erkal D., Belokurov V., 2016, MNRAS, 461, 2212 (J16)
Kallivayalil N., van der Marel R. P., Besla G., Anderson J., Alcock C., 2013, ApJ, 764, 161
Kim D., Jerjen H., 2015a, ApJ, 799, 73
Kim D., Jerjen H., 2015b, ApJ, 808, L39
Kim D., Jerjen H., Milone A. P., Mackey D., Da Costa G. S., 2015, ApJ, 803, 63
Kim D., Jerjen H., Mackey D., Da Costa G. S., Milone A. P., 2016, ApJ, 820, 119
Koposov S. et al., 2008, ApJ, 686, 279
Koposov S. E., Belokurov V., Torrealba G., Evans N. W., 2015, ApJ, 805, 130
Koposov S. E., Belokurov V., Torrealba G., 2017, MNRAS, 470, 2702
Laevens B. P. M. et al., 2015, ApJ, 813, 44
Lafler J., Kinman T. D., 1965, ApJS, 11, 216
Luque E. et al., 2016, 458, 603
Luque E. et al., 2017, MNRAS, 458, 97
Martin N. F., de Jong J. T. A., Rix H.-W., 2008, ApJ, 684, 1075
Martin N. F. et al., 2015, ApJ, 804, L5
Martin N. F. et al., 2016, ApJ, 830, L10
McConnachie A. W., 2012, AJ, 144, 4
Mohr J. J. et al., 2012, in Ellerbroek B. L., Marchetti E., Vran J.-W., eds, Proc. SPIEConf. Ser. Vol. 8451, Adaptive Optics Systems III. SPIE, Bellingham, p. 84510D
Muñoz R. R. et al., 2006, ApJ, 649, 201
Muñoz R. R., Geha M., Côté P., Vargas L. C., Santana F. A., Stetson P., Simon J. D., Djorgovski S. G., 2012, ApJ, 753, L15
Nichols M., Colless J., Colless M., Bland-Hawthorn J., 2011, ApJ, 742, 110
Nidever D. L., Majewski S. R., Burton W. B., 2008, ApJ, 679, 432
Nidever D. L., Majewski S. R., Butler Burton W., 2008, ApJ, 679, 432
Oosterhoff P. T., 1939, The Observatory, 62, 104
Pritzl B. J., Venn K. A., Irwin M., 2005, AJ, 130, 2140
Sales L. V., Navarro J. F., Cooper A. P., White S. D. M., Frenk C. S., Helmi A., 2011, MNRAS, 418, 648
Sales L. V., Navarro J. F., Kallivayalil N., Frenk C. S., 2017, MNRAS, 465, 1879
Sand D. J., Strader J., Willman B., Zaritsky D., McLeod B., Caldwell N., Seth A., Olszewski E., 2012, ApJ, 756, 79
Schlafly E. F., Finkbeiner D. P., 2011, ApJ, 737, 103
Schlegel D. J., Finkbeiner D. P., Davis M., 1998, ApJ, 500, 525
Sesar B. et al., 2010, ApJ, 708, 717
Sevilla I. et al., 2011, preprint (arXiv:1109.6741)
Springel V. et al., 2008, MNRAS, 391, 1685
Taylor M. B., 2006, in Gabriel C., Arviset C., Ponz D., Enrique S., eds., ASP Conf. Ser. Vol. 351, Astronomical Data Analysis Software and Systems XV. Astron. Soc. Pac., San Francisco, p. 666
Torrealba G., Koposov S. E., Belokurov V., Irwin M., 2016a, MNRAS, 459, 2370
Torrealba G. et al., 2016b, MNRAS, 463, 712
Vivas A. K. et al., 2016, AJ, 151, 118
Vivas A. K. et al., 2017, AJ, 154, 85
Weisz D. R. et al., 2016, ApJ, 822, 32
Wetzel A. R., Deason A. J., Garrison-Kimmel S., 2015, ApJ, 807, 49
York D. G. et al., 2000, AJ, 120, 1579
Zacharias N., Finch C. T., Girard T. M., Henden A., Bartlett J. L., Monet D. G., Zacharias M. I., 2013, AJ, 145, 44
Zinn R., Horowitz B., Vivas A. K., Baltay C., Ellman N., Hadjiyska E., Rabinowitz D., Miller L., 2014, ApJ, 781, 22

APPENDIX: OTHER PERIODIC VARIABLE STARS

Table A1 contains information about the other 46 periodic variables detected in the field of view of Carina II and Carina III. The table contains ID, RA, DEC, period (in days), and amplitudes and mean magnitudes in *gri*. Note that all but one of these stars are well outside the half-light radius of the dwarf galaxies and hence, they are expected to be non-members. Eclipsing binary star MagLiteS_J073833.89-575638.1 is located within the $r_{\rm h}$ of Car III but with no distance information is not possible to know if it is a member or just a chance alignment.

Table A1. Other periodic variable stars in the FoV of Carina II and Carina III.

ID	RA (deg)	DEC (deg)	Period (d)	Δ_g (mag)	g (mag)	Δ_r (mag)	r (mag)	Δ_i (mag)	i (mag)
MagLiteS_J073209.60-575646.6	113.040017	−57.94629	0.34764	0.55	16.61	0.58	15.81	0.57	15.50
MagLiteS_J073229.74-581043.7	113.123937	−58.17880	0.31109	0.30	19.07	0.28	18.29	0.29	17.97
MagLiteS_J073308.82-575340.8	113.286750	−57.89467	0.37512	0.17	15.85	0.13	15.25	0.12	15.05
MagLiteS_J073315.25-580605.3	113.313540	−58.10146	0.14089	0.47	20.70	0.34	20.08	0.33	19.84
MagLiteS_J073338.14-574857.0	113.408910	−57.81583	0.24591	0.33	16.05	0.31	15.58	0.27	15.43
MagLiteS_J073343.66-574518.9	113.431901	−57.75524	0.32403	0.52	19.29	0.46	18.73	0.46	18.54
MagLiteS_J073352.46-575711.6	113.468576	−57.95322	0.31856	0.17	15.86	0.15	15.28	0.12	15.07
MagLiteS_J073358.11-575602.6	113.492139	−57.93406	0.15833	0.48	19.73	0.35	19.21	0.33	19.01
MagLiteS_J073411.65-580359.4	113.548545	−58.06649	0.28094	0.31	17.28	0.29	16.49	0.27	16.20
MagLiteS_J073436.50-574947.2	113.652064	−57.82979	0.41484	0.59	16.77	0.57	16.55	0.56	16.51
MagLiteS_J073438.78-573033.0	113.661576	−57.50917	0.13799	0.29	19.70	0.28	19.50	0.28	19.44
MagLiteS_J073444.44-580138.4	113.685159	−58.02732	0.21889	0.66	20.78	0.48	19.89	0.46	19.49
MagLiteS_J073445.13-572631.7	113.688024	−57.44215	0.51143	0.22	19.92	0.12	18.97	0.08	18.53
MagLiteS_J073445.91-581713.8	113.691294	−58.28718	0.35835	0.31	17.10	0.28	16.56	0.28	16.36
MagLiteS_J073446.35-574922.2	113.693109	−57.82283	0.13254	0.44	20.35	0.19	19.76	0.18	19.53
MagLiteS_J073455.00-582253.4	113.729169	−58.38151	0.28621	0.32	15.71	0.18	14.98	0.07	14.69
MagLiteS_J073456.15-582211.3	113.733964	−58.36981	0.24194	0.84	20.48	0.69	19.67	0.60	19.31
MagLiteS_J073517.69-581601.2	113.823704	−58.26699	0.09856	0.69	21.25	0.20	19.88	0.12	18.47
MagLiteS_J073534.40-582831.7	113.893341	−58.47547	0.17787	0.17	16.45	0.20	15.95	0.25	15.75
MagLiteS_J073534.91-573536.5	113.895441	−57.59348	0.29199	0.35	16.47	0.31	15.78	0.29	15.53
MagLiteS_J073545.82-581924.6	113.940909	−58.32349	0.16011	0.47	19.97	0.38	19.50	0.36	19.31
MagLiteS_J073553.27-574817.0	113.971944	−57.80472	0.36437	0.18	17.77	0.18	16.82	0.15	16.42
MagLiteS_J073553.50-582733.0	113.972928	−58.45918	0.31909	0.61	16.78	0.56	15.98	0.60	15.67
MagLiteS_J073600.03-574943.4	114.000142	−57.82873	0.84832	0.33	20.26	0.15	19.21	0.10	18.67
MagLiteS_J073602.86-574253.9	114.011936	−57.71496	0.41908	0.22	16.43	0.22	16.24	0.22	16.19
MagLiteS_J073606.31-572307.8	114.026309	−57.38550	0.16410	0.12	18.73	0.08	18.15	0.09	17.92
MagLiteS_J073632.63-573340.7	114.135944	−57.56131	0.12280	0.12	18.81	0.13	18.37	0.11	18.20
MagLiteS_J073647.17-574048.3	114.196551	−57.68009	0.33026	0.35	17.38	0.32	16.95	0.31	16.80
MagLiteS_J073648.26-573927.9	114.201102	−57.65775	0.55454	0.04	16.88	0.06	16.52	0.07	16.38
MagLiteS_J073650.52-582740.4	114.210494	−58.46122	0.52147	0.07	15.18	0.05	14.94	0.04	14.87
MagLiteS_J073804.20-580333.0	114.517499	−58.05918	0.22999	0.64	18.93	0.55	18.29	0.52	18.01
MagLiteS_J073810.46-574918.3	114.543573	−57.82174	0.51672	0.16	18.78	0.09	17.91	0.06	17.51
MagLiteS_J073821.55-582008.1	114.589793	−58.33559	0.60013	0.20	16.27	0.20	15.96	0.18	15.85
MagLiteS_J073822.83-581014.3	114.595108	−58.17065	0.16625	0.08	16.74	0.07	16.22	0.07	16.02
MagLiteS_J073833.89-575638.1	114.641226	−57.94392	0.40344	0.30	17.78	0.29	17.58	0.28	17.51
MagLiteS_J073836.83-573145.3	114.653445	−57.52924	0.62020	0.15	19.18	0.11	17.65	0.05	16.03
MagLiteS_J073839.72-581204.0	114.665516	−58.20111	0.73806	0.20	19.30	0.11	17.97	0.08	17.19
MagLiteS_J073854.81-575850.1	114.728357	−57.98058	0.18207	0.06	16.46	0.06	15.84	0.04	15.60
MagLiteS_J073858.32-573235.9	114.743007	−57.54331	0.12879	0.55	20.65	0.47	20.13	0.49	19.87
MagLiteS_J073929.74-580919.2	114.873913	−58.15533	0.30193	0.48	15.61	0.41	15.13	0.40	14.97
MagLiteS_J073938.11-575559.8	114.908805	−57.93327	0.31649	0.38	19.94	0.30	19.89	0.25	19.90
MagLiteS_J073939.86-580725.0	114.916064	−58.12360	0.11462	0.60	20.59	0.53	19.97	0.44	19.67
MagLiteS_J073944.42-573525.9	114.935070	−57.59054	0.16329	0.55	18.64	0.52	18.17	0.49	17.96
MagLiteS_J073959.52-581942.9	114.997995	−58.32859	0.51790	0.27	20.08	0.14	18.81	0.09	18.19
MagLiteS_J074018.19-575809.8	115.075801	−57.96939	0.30735	0.32	18.81	0.28	18.18	0.28	17.92
MagLiteS_J074036.92-575337.5	115.153840	−57.89374	0.27687	0.19	18.09	0.17	17.31	0.15	17.01

[1]*Institute of Astronomy, University of Cambridge, Madingley Road, Cambridge, CB3 0HA, UK*

[2]*Institute of Astronomy and Astrophysics, Academia Sinica, PO Box 23-141, Taipei 10617,Taiwan*

[3]*Center for Computational Astrophysics, Flatiron Institute, 162 5th Avenue, New York, NY 10010, USA*

[4]*McWilliams Center for Cosmology, Department of Physics, Carnegie Mellon University, 5000 Forbes Avenue, Pittsburgh, PA 15213, USA*

[5]*Large Synoptic Survey Telescope, 950 North Cherry Avenue, Tucson, AZ 85721, USA*

[6]*Fermi National Accelerator Laboratory, PO Box 500, Batavia, IL 60510, USA*

[7]*National Optical Astronomy Observatory, 950 N. Cherry Ave., Tucson, AZ 85719, USA*

[8]*Cerro Tololo Inter-American Observatory, National Optical Astronomy Observatory, Casilla 603, La Serena, Chile*

[9]*Fermi National Accelerator Laboratory, P.O. Box 500, Batavia, IL 60510, USA*

[10]*Research School of Astronomy & Astrophysics, Mount Stromlo Observatory, Cotter Road, Weston Creek, ACT 2611, Australia*

[11]*Instituto de Astrofísica de Canarias, La Laguna, E-38205 Tenerife, Spain*

[12]*Departamento de Astrofísica, Universidad de La Laguna, E-38200 Tenerife, Spain*

[13]*Department of Astronomy, University of Illinois, 1002 W. Green Street, Urbana, IL 61801, USA*

[14]*National Center for Supercomputing Applications, 1205 West Clark St., Urbana, IL 61801, USA*

[15]*Event Horizon Telescope, Harvard-Smithsonian Center for Astrophysics, MS-42, 60 Garden Street, Cambridge, MA 02138, USA*
[16]*Australian Astronomical Observatory, North Ryde, NSW 2113, Australia*
[17]*Observatoire astronomique de Strasbourg, Université de Strasbourg, CNRS, UMR 7550, 11 rue de l'Université, F-67000 Strasbourg, France*
[18]*Max-Planck-Institut für Astronomie, Königstuhl 17, D-69117 Heidelberg, Germany*
[19]*Astronomisches Rechen-Institut, Zentrum fur Astronomie, Universitat Heidelberg, Monchhofstr. 12-14, D-69120 Heidelberg, Germany*
[20]*Department of Physics, University of Surrey, Guildford, GU2 7XH, UK*

[21]*Observatories of the Carnegie Institution for Science, 813 Santa Barbara St., Pasadena, CA 91101, USA*
[22]*Center for Astrophysics and Space Astronomy, University of Colorado, 389 UCB, Boulder, CO 80309-0389, USA*

This paper has been typeset from a TEX/LATEX file prepared by the author.